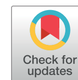

Operando characterization of conductive filaments during resistive switching in Mott VO_2

Shaobo Cheng[a,1], Min-Han Lee[b,c,1], Xing Li[a,d], Lorenzo Fratino[e], Federico Tesler[f], Myung-Geun Han[a], Javier del Valle[c,2], R. C. Dynes[c], Marcelo J. Rozenberg[e], Ivan K. Schuller[b,c], and Yimei Zhu[a,3]

[a]Department of Condensed Matter Physics and Materials Science, Brookhaven National Laboratory, Upton, NY 11973; [b]Materials Science and Engineering Program, University of California San Diego, La Jolla, CA 92093; [c]Department of Physics, Center for Advanced Nanoscience, University of California San Diego, La Jolla, CA 92093; [d]School of Physics and Microelectronics, Key Laboratory of Material Physics, Zhengzhou University, Zhengzhou, Henan, 450052, People's Republic of China; [e]Laboratoire de Physique des Solides, CNRS, Université Paris-Sud, Université Paris-Saclay, 91405 Orsay, France; and [f]Department of Integrative and Computational Neuroscience, Paris-Saclay Institute of Neuroscience, CNRS, 91198 Gif-sur-Yvette, France

Edited by Laura H. Greene, Florida State University, Tallahassee, FL, and approved January 17, 2021 (received for review July 6, 2020)

Vanadium dioxide (VO_2) has attracted much attention owing to its metal–insulator transition near room temperature and the ability to induce volatile resistive switching, a key feature for developing novel hardware for neuromorphic computing. Despite this interest, the mechanisms for nonvolatile switching functioning as synapse in this oxide remain not understood. In this work, we use in situ transmission electron microscopy, electrical transport measurements, and numerical simulations on Au/VO_2/Ge vertical devices to study the electroforming process. We have observed the formation of V_5O_9 conductive filaments with a pronounced metal–insulator transition and that vacancy diffusion can erase the filament, allowing for the system to "forget." Thus, both volatile and nonvolatile switching can be achieved in VO_2, useful to emulate neuronal and synaptic behaviors, respectively. Our systematic *operando* study of the filament provides a more comprehensive understanding of resistive switching, key in the development of resistive switching-based neuromorphic computing.

nonvolatile switching | transmission electron microscopy | conductive filament | neuromorphic computing

The development of smaller, faster, and more energy-efficient resistive switching devices with multifunctions is crucial for realizing neuromorphic computing systems. In these, "neurons" (neuristors) are active components which produce nonlinear electric signals under external excitations, while the "synapses" (synaptors) control the connectivity between active elements (1). The challenge in developing a brainlike computing hardware is to mimic and integrate these active components and their interconnections using electronic devices. Two different classes of materials are generally proposed to emulate neurons and synapses. Correlated insulators with metal–insulator transitions (such as vanadium dioxide [VO_2] or NbO_2) commonly feature threshold or volatile resistive switching: the transition to the metallic state can be induced by applying a voltage, and the device returns to the insulating state once the stimulus is removed. This makes them ideal candidates for reproducing neural spiking (2). On the other hand, many noncorrelated systems, such as TiO_2, HfO_x, or phase-change materials, are well known for having reversible nonvolatile resistive switching, very promising for implementing synaptic behavior (3). In the case of oxides, this switching is due to the drift of oxygen vacancies under strong electric fields. Moreover, to improve the processing speed, scalability, device density, and connectivity like those in biological systems, the development of three-dimensional (3D) cross-bar circuit is necessary (4, 5). However, fabrication of 3D stacked arrays is difficult and further studies on vertical resistive switching devices will be required.

Among the different materials, VO_2 has attracted much attention because of its threshold switching behavior and its insulator–metal transition (IMT) near room temperature (6–11). The mechanism behind the volatile switching in VO_2 is believed to be a combination of thermal and/or electrical field-induced IMT in response to an external voltage/current input (12–15). However, unlike other transition-metal oxides such as TiO_2 (16, 17), the microscopic nature of the electroforming process and nonvolatile switching behavior in the Mott insulator VO_2 has not yet been explored (18). Interestingly, this provides the opportunity to realize nonvolatile resistive switching (caused by oxygen vacancy migration) coexisting with volatile resistive switching. This is of great potential, since the same material can show both neuronlike and synapselike functionalities. The nanoscale nature of the conductive filament poses a major challenge to the study of the nonvolatile switching mechanism (19). Here, combining *operando* transmission electron microscopy (TEM), transport measurements, and numerical simulations, we elucidate the electroforming process in Au/VO_2/Ge vertical devices. The *operando* TEM studies allow us to conduct simultaneous structural and transport characterizations. The atomic structure of the nanoscale conductive filament was unambiguously determined and a filament relaxation/recovery mechanism has been demonstrated. Our study unveiled the essential role of oxygen defects in the filament formation and relaxation during resistive switching.

Significance

To perform hardware-based neuromorphic computing, novel materials exhibiting a wide variety of electronic properties are currently being explored. VO_2 is well known to exhibit an insulator-to-metal transition as well as volatile resistive switching. Many questions regarding the basic mechanism of the nonvolatile switching in this material are unanswered. In this work, the formation and relaxation of conductive filaments through nonvolatile resistive switching in VO_2 devices have been realized. The V_5O_9 Magnéli phase conductive filament has been identified. Our results demonstrate that both resistive switching behaviors can be achieved in a single material, crucial for future technology like resistive switching memories or neuromorphic logic.

Author contributions: S.C., M.-H.L., X.L., I.K.S., and Y.Z. designed research; S.C., M.-H.L., X.L., L.F., F.T., M.-G.H., J.d.V., R.C.D., and M.J.R. performed research; S.C., M.-H.L., I.K.S., and Y.Z. analyzed data; and S.C., M.-H.L., and L.F. wrote the paper.

The authors declare no competing interest.

This article is a PNAS Direct Submission.

Published under the PNAS license.

[1]S.C. and M.-H.L. contributed equally to this work.

[2]Present Addresses: Department of Quantum Matter Physics, University of Geneva, 24 Quai Ernest-Ansermet, 1211 Geneva, Switzerland.

[3]To whom correspondence may be addressed. Email: zhu@bnl.gov.

This article contains supporting information online at https://www.pnas.org/lookup/suppl/doi:10.1073/pnas.2013676118/-/DCSupplemental.

Published February 23, 2021.

APPLIED PHYSICAL SCIENCES

Results and Discussion

Fig. 1*A* shows a 150-nm VO_2 thin film deposited onto a Ge substrate by magnetron sputtering. The single-phase growth of the (011) VO_2 polycrystalline thin film was confirmed by X-ray diffraction (*SI Appendix*, Fig. S1) (20). The Ga-doped Ge substrate has p-type conductivity with a room temperature resistivity of 0.001 Ohms·cm. To investigate the resistive switching behavior, a VO_2 layer sandwiched between two electrodes (Au as top electrode and highly doped Ge as bottom electrode as shown in Fig. 1*A*) was fabricated. Fig. 1*B* shows the thermal-induced IMT for one of the Au/VO_2/Ge devices with a transition temperature, T_{IMT} ~345 K. This device exhibits a nearly three order of magnitude resistance change with a 10 K heating–cooling thermal hysteresis. The atomic unit cell of the low-temperature monoclinic insulating phase (noted as M1 phase) and the high-temperature rutile metallic phase are shown in the insets. Volatile resistive switching can be found for the Au/VO_2/Ge devices when their temperature is raised close to the T_{IMT} (*SI Appendix*, Fig. S2). The VO_2 returns to the insulating state upon removing the external current. The mechanism of this switching has been studied earlier and is due to a combination of thermal (12–14) and/or nonthermal (15) switching depending on the details of the defects present.

Fig. 1*C* shows the I-V curve measured at room temperature, featuring clear nonvolatile resistive switching. As the current increases to the threshold value, a large drop of the voltage indicates the formation of the low-resistance state between the two electrodes. The subsequent temperature-dependent transport measurement of this device reveals another insulator–metal transition around 140 K with a 50 K-wide thermal hysteresis. Moreover, this IMT shows a resistive asymmetry between the heating and cooling branches. The broadening of the hysteresis and the asymmetry in the R-T curve have been observed in many one-dimensional correlated oxide systems (21, 22). In addition, like other transition-metal oxides (1, 18, 23), oxygen migration in VO_2 may lead to the formation of oxygen-deficient filaments. Thus, the pronounced IMT with several orders of magnitude resistance change might be associated with an oxygen-deficient vanadate phase within the VO_2 film. Due to the multiple possible vanadium oxidation states, a whole oxide family known as Magnéli (V_nO_{2n-1}) and Wadsley phases (V_nO_{2n+1}) (24) are stable. Among these compounds, only V_2O_3, V_5O_9, and V_6O_{11} have lower oxygen/vanadium ratios than VO_2 with an IMT near 140 K. This implies that these VO_{2-x} phases are possibly formed during the resistive switching within the VO_2 film.

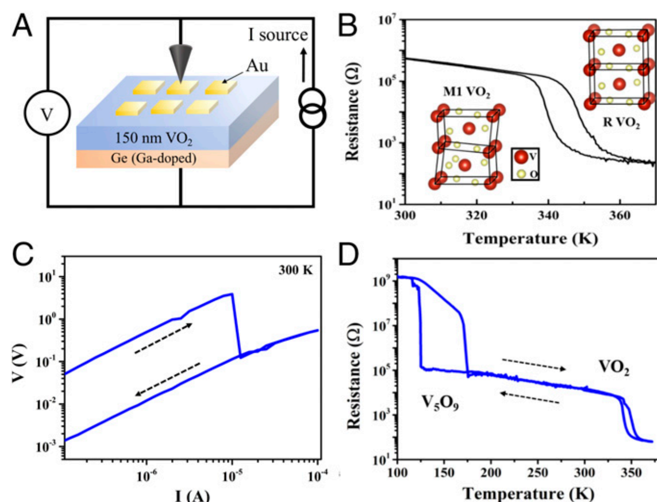

Fig. 1. Nonvolatile resistive switching in Au/VO_2/Ge vertical devices. (*A*) Schematic illustration of the out-of-plane VO_2 device and the measurement setup. The Au and highly doped Ge are top and bottom electrodes, respectively. (*B*) Resistance as a function of temperature of 150-nm VO_2 film. (*Inset*) Low-temperature insulating VO_2 monoclinic phase (M1 VO_2) and high-temperature metallic VO_2 rutile phase (R VO_2). (*C*) Room-temperature I-V curve. (*D*) After electroforming, the R-T curve of the VO_2 device shows another metal-insulator transition behavior at low temperatures.

To understand the nonvolatile switching mechanism and gain insights into the filament formation, in situ biasing TEM experiments were carried out. The experimental setup is shown in Fig. 2*A*. All the experimental images in Fig. 2 are scanning transmission electron microscopy high-angle annular dark-field (STEM-HAADF) images, which are sensitive to the atomic weight in the sample (25). As illustrated in Fig. 2*B*, the top Au and Pt layers are the protection layers deposited during FIB (focused ion beam) process and used as top electrode in the biasing experiments. The sample was separated into two independent out-of-plane devices by three vertical FIB cuts. The piezocontrolled W tip was grounded and made a contact with the top Pt layer. A live view of the device with different applied voltages was captured and is shown in Movie S1. While sweeping the voltage from 0 to 3 V, the conductive filament becomes visible as the dark regions in the image. The STEM images showing the changes of the sample are in *SI Appendix*, Fig. S3. Fig. 2*C* depicts the morphology of the conductive filament and the corresponding schematic representation of the conductive filament is shown. The selected area electron diffraction (SAED) pattern acquired from the filament area (the actual selected area on the sample is about 100 nm in diameter) is shown in Fig. 2*D*. Together with the electron diffraction peaks from the M1 VO_2 phase (the electron diffraction pattern for the pure M1 VO_2 can be found in *SI Appendix*, Fig. S4), an additional set of diffraction peaks with about 1/3 of the reciprocal lattice spacing of VO_2 along the *a* axis (indicated by red arrows) is observed. This is identified as the V_5O_9 phase. The simulated SAED patterns captured along M1 VO_2 [010] and [102], as well as V_5O_9 [120] directions, are shown in *SI Appendix*, Fig. S5, which match well with the experimental diffraction pattern in Fig. 2*D*. Considering the lattice symmetry, both the M1 VO_2 and V_5O_9 phases have structural variants, i.e., twinning. A diffraction mirror plane can be identified. Using the diffraction spot from the V_5O_9 phase, as indicated by the red circle in Fig. 2*D*, a dark-field TEM image was acquired (Fig. 2*E*), showing the distribution of the newly formed V_5O_9 phase. The shape of the conductive filament is consistent with that shown in Fig. 2*C*, showing that the conductive filament is composed of V_5O_9 phase. The high-resolution TEM image acquired from the filament area is shown in *SI Appendix*, Fig. S6. The dark-field TEM image also shows some isolated V_5O_9 nanograins (within tens of nanometer in size) near the conductive filament formed during the electroforming process. The region identified as conductive filament is within a VO_2 matrix. It is noteworthy to mention that V_5O_9 phase also shows a first-order IMT (the transition temperature is about 135 K), consistent with the low-temperature IMT shown in Fig. 1*D* (26, 27). Electron energy-loss spectroscopy (EELS) results also reveal the change of V valence state in the conductive filament area (28). Since the $L_{2,3}$ edges of V are very close to the O K edge, L_3 and L_2 area ratios cannot be used to extract the valence state of V (10). However, the change of valence states could affect the number of screening electrons around the nucleus, thus resulting in a change in the onsite energy of the L_3 edge. Furthermore, considering the VO_6 octahedral coordination, the lowest unoccupied state should change as well, which should be reflected in the oxygen K edge. Fig. 2*F* shows a 0.15 eV redshift in energy for the V_5O_9 phase, which is an indication for the decrease of the V valence state and the stoichiometry change (27). The energy positions for π^*, σ^*, $d_{//}$ orbitals in the VO_2 EELS spectrum can be identified in oxygen K edge, which is consistent with X-ray results (29). In V_5O_9 phase, the formation of oxygen vacancy

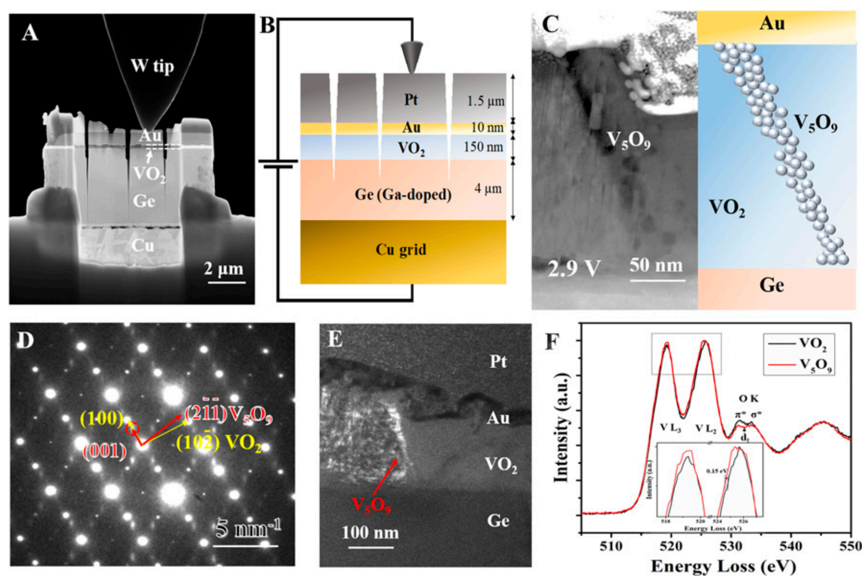

Fig. 2. *Operando* TEM studies showing the formation of conductive filament. (*A* and *B*) HAADF image and schematic diagram of the experimental setup of the VO_2 device. Each FIB sample has three vertical cuts, making two out-of-plane devices. (*C*) Experimental image and the corresponding schematic of the conductive filament. (*D*) SAED acquired from the conductive filament area. (*E*) Dark-field image using the diffraction spot marked by red circle ((001) of V_5O_9) in *D*. (*F*) Core-loss EELS for VO_2 and V_5O_9. Approximately 0.15-eV energy shift is found for the V_5O_9.

increases the occupation of the π^* orbital and thus the first peak in the oxygen K edge should decrease. Since V_5O_9 is conductive at room temperature, its orbital diagram can be deduced from an analysis of the orbital hybridization (see *SI Appendix*, Fig. S7 for details) (10).

The mechanism of oxygen migration and the switching reversibility can be further studied by thermally annealing the device after the nonvolatile filament formation. Transport properties of strongly correlated oxides, such as VO_2 and V_5O_9, are extremely sensitive to the variation in oxygen content, carrier density, and structural disorder (30). Fig. 3*A* shows the R-T curve of the V_5O_9 filament after the IV switching (blue curve), after annealing in air for 30 min (green) and 1 h (red) at 400 K. The R-T curve changes dramatically, showing the recovery from V_5O_9 to the original VO_2 state as a result of the reoxidation of the filament during annealing. The resistance in the low-temperature region increases with longer annealing time associated with a degradation of the V_5O_9 IMT, indicating the

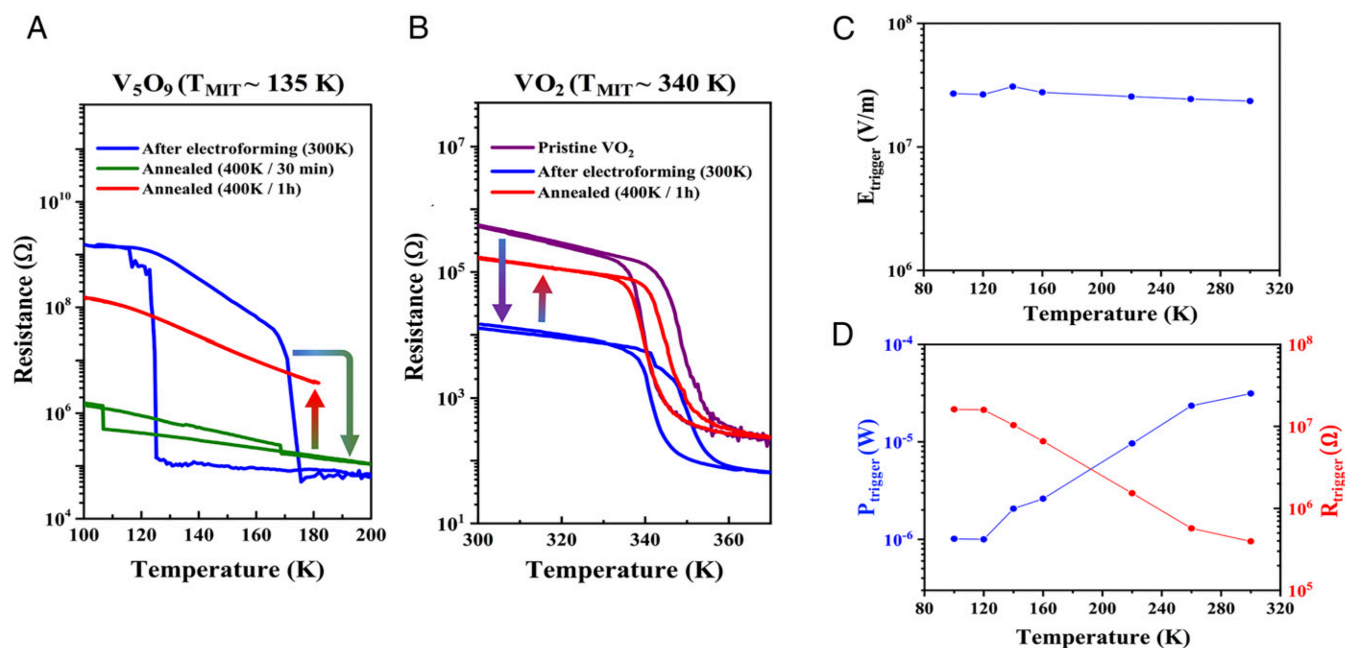

Fig. 3. Relaxation of the nanoscale filament in VO_2. (*A*) R vs. T for a device at low temperatures: after the nonvolatile resistive switching (blue); after thermal annealing for 30 min at 400 K in air (green); after thermal annealing for 1 h at 400 K in air (red). (*B*) R vs. T curve for a device at high temperature: pristine VO_2 device (purple); after nonvolatile resistive switching (blue); after thermal annealing for 1 h at 400 K in air (red). (*C*) Breakdown electrical field as a function of device temperature. (*D*) Power dissipation ($P_{trigger}$) and switching resistance ($R_{trigger}$) as a function of device temperature for VO_2 nonvolatile switching.

disappearance of this Magnéli phase. It may be worthwhile to mention that small change along the filament length could result in a large change in the total resistance, making the low-temperature IMT signal appear to be strong. The R-T measurements at high temperature reveal the VO_2 IMT, as shown in Fig. 3*B*. After the V_5O_9 filament forming, the magnitude of the VO_2 IMT is slightly reduced. This electroforming process is likely to increase the density of oxygen vacancies and lead to oxygen loss from the VO_2 monoclinic structure. These vacancies behave as electron donors in the original VO_2, thereby increasing the number of free-charge carriers and reducing the magnitude of the IMT. After annealing, the VO_2 will partially recover to the original state. The reduced resistive change and the decrease in the hysteresis loop width across the IMT indicate further the presence of the oxygen-deficient phase.

The breakdown electric field of the nonvolatile filamentary switching is temperature independent at nearly ∼28 MV/m (Fig. 3*C*). Moreover, the power needed to induce nonvolatile switching increases with increasing device temperature (Fig. 3*D*). This is inconsistent with pure Joule heating-triggered behavior and indicates the presence of oxygen migration, as described before (31). On the other hand, triggering the volatile resistive switching at high temperature ($\sim T_{IMT}$) may be dominated by local Joule heating. In this case, the power dissipation and threshold voltage are expected to decrease with increasing device temperature (32). The temperature dependence of the breakdown electric field will be significant. These results show that both volatile and nonvolatile resistive switching can be realized, but as evidenced by the very different T dependence, caused by different mechanisms in the Au/VO_2/Ge vertical geometry.

Using the experimental setup shown in Fig. 4*A*, the reversibility of the conductive filament in Au/VO_2/Ge vertical device was studied in TEM. The compliance current was limited to 0.1 mA and the first "set process" is shown in black in Fig. 4*D*. The IV curve was measured simultaneously while recording the TEM images, as shown in Fig. 2. The device has high resistance initially and the current increases sharply with the application of 2.8 V. The sample resistance decreases markedly with the formation of the conductive filament as illustrated in Fig. 4 *E* and *F*. This in situ biasing measurement agrees well with the ex situ device measurement shown in Fig. 1*C*. After the biasing experiments, the sample was annealed in air at 400 K for 30 min to test its reversibility. Fig. 4*B* shows the morphology of conductive filament after partial recovery. The dark areas clearly decreased compared with those shown in Fig. 2*C*. The V_5O_9 phase returns to VO_2 during annealing in air, showing the reversibility of the nonvolatile resistive switching. The second test was applied under the same condition on the recovered sample, and the IV curve is shown in red in Fig. 4*D*. Similar to the first measurement, the sample shows high-resistance state and changes to low-resistance state at 2.6 V. The change of voltage decreases slightly, due to the remaining V_5O_9 phase in the recovered sample, as illustrated in Fig. 4*G*. The snapshot after the second switching experiment (videos can be found in Movie S2) is shown in Fig. 4*C*, showing the formation of the conductive filament. The new filament appears at the same position of the old one, indicating that the filament has a "memory effect." However, the diameter of the filament becomes bigger, as illustrated in Fig. 4*H*, which is consistent with the lower-resistance state in the second measurement. From the TEM measurements, we found that the conductive filaments form in a randomly fashion between the top and bottom parallel electrodes. It is possible that the local defects, such as oxygen vacancies, grain boundaries, domain boundaries may facilitate filament formation, and further exploration is needed. Based on our He^+ ions injection simulations, it is also possible to control the formation of Magnéli phase and create conductive filaments (details of which can be found in *SI Appendix*).

To deepen the understanding about the formation and relaxation of the conductive filament in the volatile and nonvolatile switching (11, 33), numerical simulations using Mott resistors network model were performed as illustrated in *SI Appendix*, Fig. S8. A load resistance R_{load} is making a voltage divider circuit with a resistor network, where each resistor takes the resistance values of rutile VO_2, M1 VO_2, or V_5O_9. At different temperatures, the competition between two insulator–metal transitions produces a

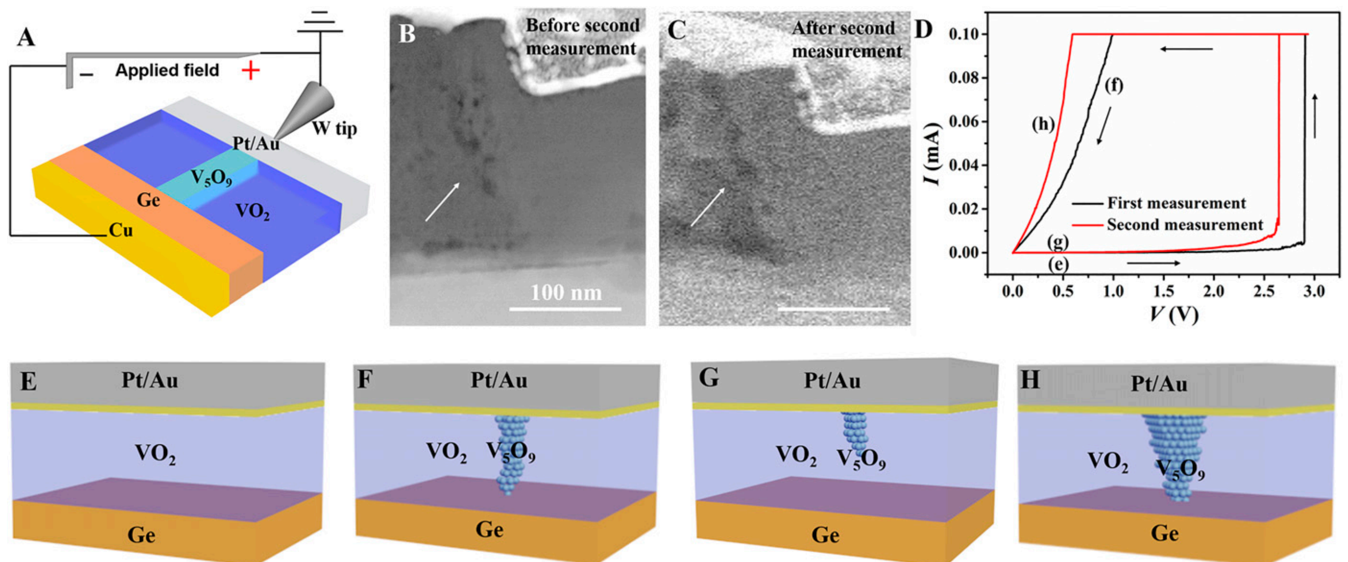

Fig. 4. Reversibility of the nonvolatile resistive switching. (*A*) The schematic showing the formation of V_5O_9 conductive filament under external bias. (*B*) HAADF-STEM showing the morphology of the conductive filament after recovery. (*C*) Formation of the conductive filament at the same position after second biasing experiment. (*D*) IV curve measured in situ in the TEM. The black and red curves show the IV results for the first and second measurement, respectively. For the first measurement, the initial state is illustrated in *E*. The low-resistance state after electroforming process is shown in *F*. After the recovery, the partially survived filament is plotted in *G*, which is the starting state for the second measurement. The final state with the formation of thicker conductive filament after second switching is demonstrated in *H*.

volatile transition driven by Joule heating predominant when T approaches T_{IMT} and a nonvolatile transition associated with a structural transition that dominates at T well below T_{IMT}, activated by the local electric field. Near the IMT (338 K), the system shows volatile switching and the conductive filament is mainly formed by rutile VO_2 as shown in *SI Appendix*, Fig. S9. At low temperature (280 K) shown in *SI Appendix*, Fig. S10, the system exhibits nonvolatile switching and the conductive filament is made of V_5O_9 phase. V_{th} is the threshold voltage that triggers volatile switching.

In Fig. 5, we present the room-temperature simulations. Applying an above-threshold pulse (the applied voltage is 1.25 times of threshold voltage, i.e., $V_{app}/V_{th} = 1.25$), a V_5O_9 (red color in Fig. 5*E*) filament is created by voltage activation together with a partially metallic VO_2 (green in Fig. 5*E*) produced by Joule heating. The threshold voltage (V_{th}) is the minimum value able to let the transition from the metallic to the insulating state beginning from a given temperature and letting the voltage act for long time. While rutile VO_2 fraction relaxes back to its insulating state (11), after the pulse ends, the V_5O_9 persists unchanged (Fig. 5*F*). The annealing process can be simulated by increasing the substrate temperature to 620 K after the creation of the filament. The V_5O_9 gradually turns back into metallic rutile VO_2 (Fig. 5*G*), so by cooling back the system to the initial value the conductive filament is partially recovered due to the thermal transition from rutile VO_2 to M1 VO_2 (Fig. 5*H*). The timescale for the annealing process of the V_5O_9 filament depends on the substrate temperature, i.e., a lower temperature leads to a longer relaxation time. If a second pulse below threshold ($V_{appl}/V_{th} = 0.85$) is applied after the annealing process, a V_5O_9 filament forms at the same position. This "subthreshold" effect (11) is in good agreement with earlier experimental results. The full simulated movie can be found in Movie S3.

Unlike TiO_2 (16), VO_2 exhibits a metal–insulator transition above room temperature. In TiO_2, a large reset current can be used to disrupt the conductive filament by Joule heating. However, for VO_2, it is not possible to reset the conductive path using electrical stimuli after the electroforming process. The surrounding areas of V_5O_9 conductive filament will be heated up by the current, leading to the formation of metallic rutile-phase VO_2. The large current will flow through the metallic rutile-phase VO_2 rather than accumulating enough heat for oxygen migration, which can be inferred from our simulation results shown in *SI Appendix*, Fig. S11.

Based on our experimental data and the simulation results, filament formation process can be understood by this scenario: 1) During the initial switching stage (electroforming), the oxygen vacancies start moving under the external field. Above certain oxygen vacancy level, the isolated V_5O_9 nanograins will form in some part of the VO_2 thin film. 2) Once the V_5O_9 nanograins connect between two electrodes, large current will naturally flow through the conductive pathway. The filament is shorting the rest parts of the VO_2 film which are highly insulating. The voltage/electric field will be significantly reduced after the switching and prevent further formation of other V_5O_9 conductive filament.

In conclusion, coordinated in situ and ex situ experiments using voltage bias of VO_2 show the formation of V_5O_9 conductive filaments. Besides the intrinsic volatile switching of VO_2, the nonvolatile switching can be attributed to the appearance and disappearance of the V_5O_9 Magnéli phase. These behaviors are well captured by numerical simulations of a theoretical model which provides support to the idea that two electric field-induced insulator–metal transitions are competing in VO_2. Our study identified the essential role played by the Magnéli filament within the VO_2 device. This is supported with detailed characterizations of the insulator–metal transition, phase composition,

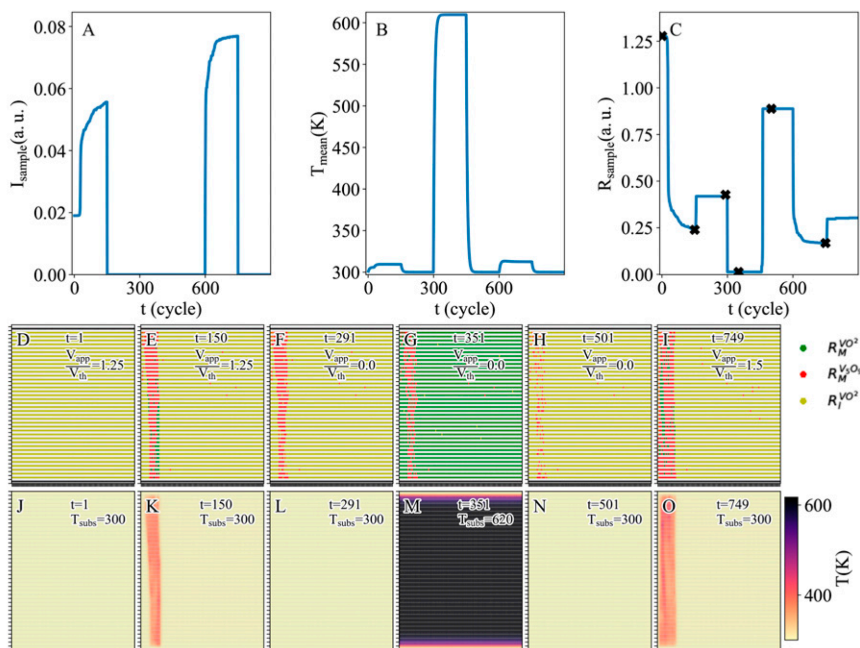

Fig. 5. Numerical simulations showing the formation and relaxation processes of conductive filaments at room temperature. (*A*) Electric current of the resistor network as a function of time. A first voltage pulse of $V_{app}/V_{th} = 1.25$ is applied from t = 1 to t = 150 and a second one of $V_{app}/V_{th} = 0.85$ is applied from t = 600 to t = 750. (*B*) Average temperature through the network as a function of time. The small variation in the sample temperature at 300 K is due to the applied voltage that induces local Joule heating. The substrate temperature is increased up to 620 K for annealing purpose at 300 < t < 450 and 750 < t < 1200. (*C*) Resistivity of the resistor network as a function of time. (*D–I*) Distributions of metallic rutile VO_2 (green), V_5O_9 phase (red), and insulator M1 VO_2 (yellow) at different stages: (*D*) t = 1 (starting position); (*E*) t = 150 (during first pulse voltage of $V_{app}/V_{th} = 1.25$); (*F*) t = 291 (after relaxation of the first pulse); (*G*) t = 351 (during the first annealing process); (*H*) t = 501 (after the first annealing process); (*I*) t = 749 (the second pulse with smaller stimuli). These different stages are marked as stars in *C*. Note, the t is the simulation step. (*J–O*) The corresponding temperature distributions in degrees Kelvin. The whole simulation is shown in Movie S3.

https://doi.org/10.1073/pnas.2013676118

lattice structure, and its relation to the surrounding VO_2. We demonstrated that two different resistive switching behaviors can be induced using Au/VO_2/Ge vertical resistive switching device. This is of great interest to emulate both neuronal and synaptic behaviors on the same material. Moreover, we have identified a filament relaxation effect that allows the system to forget. This could have crucial implications in the implementation of oxide-based devices for neuromorphic computing. Our findings could be applied to a broad range of interdisciplinary fields, including strongly correlated materials, complex oxides with IMT behavior. Also, the second IMT of the Magnéli V_5O_9 filaments is an excellent candidate for low-temperature applications. We believe this work is likely to be of great interest to researchers exploring new resistive switching oxide devices with different memory effects and modulating transport properties across metal–insulator transitions in oxide-based technology. Thus, another route for realizing neuromorphic computing has been found.

Materials and Methods

TEM Studies. The TEM studies were carried out on an FEI Talos microscope at 200 kV accelerating voltage. The in situ biasing study was carried out with an STM Nanofactory in situ biasing holder. TEM samples were fabricated by an FEI Helios dual-beam system. The samples were polished at low voltages to remove the surface damage layers at the last step of the sample preparation. A 10 μm selective-area aperture was used for acquiring electron diffraction patterns. The EELS was acquired with 0.1 eV/ch dispersion. To satisfy the selection rule, the convergence angle was 19.1 mrad and the collection angle was 39.6 mrad. The energy resolution was estimated to be 0.7 eV.

Thin-Film Growth and Device Fabrication. Polycrystalline VO_2 thin films, 150 nm thick, were grown on (100)-oriented P-type Ga-doped Ge substrates by radio frequency magnetron sputtering from a V_2O_3 target. The growth of VO_2 was done at a substrate temperature of 445 °C using an Ar/O_2 mixture (8% O_2) at 3.7 mTorr. Single-phase growth of VO_2 was confirmed by room-temperature θ-2θ X-ray diffraction using Rigaku SmartLab with Cu Kα radiation (λ = 1.54 Å) and TEM. Using e-beam evaporation and a shadow mask, 100 nm Au top electrodes for electrical transport measurements were fabricated.

Electrical Measurements. Temperature-dependent electrical transport of Au/VO_2/Ge devices were performed in a Lakeshore TTPX probe station with a Keithley 6221 current source and a Keithley 2182A nanovoltmeter in a two-point probe configuration.

Data Availability. All study data are included in the article and/or supporting information.

ACKNOWLEDGMENTS. The structural characterization, transport, *operando* TEM, and collaboration among University of California San Diego (UCSD), Brookhaven National Laboratory (BNL), and CNRS were supported through an Energy Frontier Research Center program funded by the US Department of Energy (DOE), Office of Science, Basic Energy Sciences, under Grant DE-SC0019273. Electron microscopy work at BNL and the use of BNL's Center for Functional Nanomaterials were supported by DOE-BES, the Division of Materials Science and Engineering, and the Division of Science User Facility, respectively, under Contract no. DE-SC0012704. The thin-film deposition and device fabrication were funded by the Vannevar Bush Faculty Fellowship program sponsored by the Basic Research Office of the Assistant Secretary of Defense for Research and Engineering, and by the Office of Naval Research through Grant N00014-15-1-2848.

1. J. D. Valle, J. G. Ramírez, M. J. Rozenberg, I. K. Schuller, Challenges in materials and devices for resistive-switching-based neuromorphic computing. *J. Appl. Phys.* **124**, 211101 (2018).
2. W. Yi *et al.*, Biological plausibility and stochasticity in scalable VO_2 active memristor neurons. *Nat. Commun.* **9**, 4661 (2018).
3. D. Ielmini, H.-S. P. Wong, In-memory computing with resistive switching devices. *Nat. Electron.* **1**, 333–343 (2018).
4. M. D. Pickett, G. Medeiros-Ribeiro, R. S. Williams, A scalable neuristor built with Mott memristors. *Nat. Mater.* **12**, 114–117 (2013).
5. J. J. Yang, D. B. Strukov, D. R. Stewart, Memristive devices for computing. *Nat. Nanotechnol.* **8**, 13–24 (2013).
6. Z. Shao, X. Cao, H. Luo, P. Jin, Recent progress in the phase-transition mechanism and modulation of vanadium dioxide materials. *NPG Asia Mater.* **10**, 581–605 (2018).
7. F. Morin, Oxides which show a metal-to-insulator transition at the Neel temperature. *Phys. Rev. Lett.* **3**, 34 (1959).
8. S. Kumar *et al.*, Sequential electronic and structural transitions in VO_2 observed using X-ray absorption spectromicroscopy. *Adv. Mater.* **26**, 7505–7509 (2014).
9. S. Wall *et al.*, Ultrafast disordering of vanadium dimers in photoexcited VO_2. *Science* **362**, 572–576 (2018).
10. N. B. Aetukuri *et al.*, Control of the metal-insulator transition in vanadium dioxide by modifying orbital occupancy. *Nat. Phys.* **9**, 661–666 (2013).
11. J. Del Valle *et al.*, Subthreshold firing in Mott nanodevices. *Nature* **569**, 388–392 (2019).
12. A. Zimmers *et al.*, Role of thermal heating on the voltage induced insulator-metal transition in VO2. *Phys. Rev. Lett.* **110**, 056601 (2013).
13. S. Kumar *et al.*, Local temperature redistribution and structural transition during joule-heating-driven conductance switching in VO_2. *Adv. Mater.* **25**, 6128–6132 (2013).
14. H. Madan, M. Jerry, A. Pogrebnyakov, T. Mayer, S. Datta, Quantitative mapping of phase coexistence in Mott-Peierls insulator during electronic and thermally driven phase transition. *ACS Nano* **9**, 2009–2017 (2015).
15. Y. Kalcheim *et al.*, Non-thermal resistive switching in Mott insulator nanowires. *Nat. Commun.* **11**, 2985 (2020).
16. D.-H. Kwon *et al.*, Atomic structure of conducting nanofilaments in TiO_2 resistive switching memory. *Nat. Nanotechnol.* **5**, 148–153 (2010).
17. K. Tang *et al.*, Distinguishing oxygen vacancy electromigration and conductive filament formation in TiO_2 resistance switching using liquid electrolyte contacts. *Nano Lett.* **17**, 4390–4399 (2017).
18. H.-S. P. Wong *et al.*, Metal-Oxide RRAM. *Proc. IEEE* **6**, 1951–1970 (2012).
19. W. Sun *et al.*, Understanding memristive switching via in situ characterization and device modeling. *Nat. Commun.* **10**, 3453 (2019).
20. Z. Yang, C. Ko, S. Ramanathan, Metal-insulator transition characteristics of VO_2 thin films grown on Ge (001) single crystals. *J. Appl. Phys.* **108**, 073708 (2010).
21. J. del Valle *et al.*, Resistive asymmetry due to spatial confinement in first-order phase transitions. *Phys. Rev. B* **98**, 045123 (2018).
22. W. Fan *et al.*, Large kinetic asymmetry in the metal-insulator transition nucleated at localized and extended defects. *Phys. Rev. B Condens. Matter Mater. Phys.* **83**, 235102 (2011).
23. R. Waser, M. Aono, Nanoionics-based resistive switching memories. *Nat. Mater.* **6**, 833–840 (2007).
24. U. Schwingenschlögl, V. Eyert, The vanadium Magnéli phases V_nO_{2n-1}. *Ann. Phys.* **13**, 475–510 (2004).
25. S. Cheng *et al.*, Interface reconstruction with emerging charge ordering in hexagonal manganite. *Sci. Adv.* **4**, eaar4298 (2018).
26. B. Fisher, J. Genossar, G. M. Reisner, Systematics in the metal-insulator transition temperatures in vanadium oxides. *Solid State Phys.* **226**, 29–32 (2016).
27. M. Marezio, P. D. Dernier, D. B. McWhan, S. Kachi, Structural Aspects of the metal-insulator transition in V_5O_9. *J. Solid State Chem.* **11**, 301–313 (1974).
28. H. Tan, J. Verbeeck, A. Abakumov, G. V. Tendeloo, Oxidation state and chemical shift investigation in transition metal oxides by EELS. *Ultramicroscopy* **116**, 24–33 (2012).
29. T. C. Koethe *et al.*, Transfer of spectral weight and symmetry across the metal-insulator transition in $VO_{(2)}$. *Phys. Rev. Lett.* **97**, 116402 (2006).
30. K. Liu, S. Lee, S. Yang, O. Delaire, J. Wu, Recent progresses on physics and applications of vanadium dioxide. *Mater. Today* **21**, 875–896 (2018).
31. J. del Valle *et al.*, Electrically induced multiple metal-insulator transitions in oxide nanodevices. *Phys. Rev. Appl.* **8**, 054041 (2017).
32. W. A. Vitale *et al.*, Steep-slope metal–insulator-transition VO_2 switches with temperature-stable high I_{ON}. *IEEE Electron. Device Lett.* **36**, 972–974 (2015).
33. E. Janod *et al.*, Resistive switching in Mott insulators and correlated systems. *Adv. Funct. Mater.* **25**, 6287–6305 (2015).